Journal of Applied Fluid Mechanics, Vol. 17, No. 6, pp. 1339-1353, 2024.
Available online at www.jafmonline.net, ISSN 1735-3572, EISSN 1735-3645.
https://doi.org/10.47176/jafm.17.6.2155

Numerical Simulation of Underwater Supersonic Gaseous Jets of Underwater Vehicle with Porous Media Layer

Y. Shen[1], J. Luo[2], B. Yang[1], J. Xia[2], Y. Wang[1†] and S. Li[3]

[1] *Shanghai Key Laboratory of Multiphase Flow and Heat Transfer of Power Engineering, School of Energy and Power Engineering, University of Shanghai for Science and Technology, Shanghai, China*
[2] *Shanghai Space Propulsion Technology Research Institute, Shanghai, 201109, China*
[3] *School of Aerospace Engineering, Beijing Institute of Technology, Beijing, China*

†Corresponding Author Email: wangying@usst.edu.cn

ABSTRACT

With regard to the pronounced pressure pulsation and cyclic thrust oscillation observed in the tail flow field of an underwater vehicle operating under over-expanded conditions, and drawing inspiration from flow control techniques involving porous media structures like submarine coral reefs and breakwaters, this paper presents an innovative proposition to incorporate a porous media layer on the tail wall of the nozzle in order to regulate the structure of the tail gaseous jets. To optimize the flow control of underwater vehicles, the utilization of porous media layers with varying degrees of porosity is employed to establish a model for underwater supersonic gaseous jets. This model scrutinizes the intricate structure of the tail gaseous jets, as well as the consequential wall pressure and thrust engendered by the nozzle. The findings eloquently demonstrate that the porous media model, boasting a porosity of 0.34, exerts a diminished influence on the morphological characteristics of the tail gaseous jets, while concurrently yielding a superior flow control effect on the pulsation of tail wall pressure and attenuating the differential thrust generated by the underwater vehicle. Consequently, this innovative approach effectively mitigates overall thrust oscillation, thereby enhancing the stability of the underwater vehicle throughout its submerged operations.

Article History

Received July 13, 2023
Revised December 19, 2023
Accepted January 5, 2024
Available online March 27, 2024

Keywords:

Underwater vehicle
Underwater supersonic gaseous jets
Pressure pulsation
Porous media
Flow control

1. Introduction

Underwater vehicle working underwater is a typical supersonic gaseous jets, whose working environment is very complex due to the high density and high pressure of the external water environment. Furthermore, owing to the substantial inertia of water, the emission of gas from the combustion chamber is constrained, and as the water pressure escalates, this hindrance becomes more pronounced. Moreover, the gaseous jets have the propensity to induce pressure pulsations within the tail flow domain, thereby compromising thrust efficiency and impeding the overall performance of the underwater vehicle. Consequently, it becomes imperative to delve into the investigation of nozzle flow separation triggered by substantial back pressure.

Numerous scholars, both domestic and international, have undertaken experimental measurements and numerical simulations pertaining to the realm of underwater supersonic gaseous jets. Loth and Faeth (1989) found through experiments of underwater gaseous jets that the shock structure produced by the gaseous jets is similar to that in air. Gong et al. (2017) studied the flow behavior of gas jets underwater through numerical simulation, and compared the numerical simulation results with gas jets in air. The research results showed that the greater the pressure in the external water environment, the more prone the underwater gas jet to necking and rebound phenomena, and the more unstable the jet. Tang et al. (2011) compared the experimental results with the numerical settlement results and found that there are four typical phenomena during the underwater gaseous jets process: expansion, bulging, necking, and back attack. It was also found that the pressure difference between the front and rear surfaces of the engine wall can produce additional thrust. Shi et al. (2010) studied underwater supersonic gaseous jets and found that the flow oscillations caused by supersonic jets entering water were related to the feedback phenomenon of excitation waves in the gas phase. Fronzeo and Kinzel (2016) delved into

Nomenclature			
v	velocity	ρ	density
F	the thrust produced by the engine	R	pressure fluctuation rate
n	porosity	H	height
μ	dynamic viscosity	W	width
υ	kinematic viscosity		

the intricacies of gaseous jets within liquid environments characterized by varying densities. Their investigation revealed a profound correlation between the density of the ambient fluid and the extent of jet penetration, while also noting an escalation in turbulence intensity at the gas-liquid interface as the density of the surrounding medium intensified. Li et al. (2017) examined the phenomenon of gaseous jets emerging from the outlet of an underwater vertical annular nozzle. They discovered that the shear instability of the gas jet induced a necking effect, leading to an elevation in the internal pressure of the gas and ultimately resulting in the pinch-off phenomenon of the jet. Tang et al. (2016) explored the impact of jet morphology on thrust and observed that as a consequence of the periodic bulging, necking, and back attack of the underwater gaseous jets, a multi-order frequency peak emerged in the thrust frequency spectrum. Zhang et al. (2020) employed the VOF multiphase flow model to simulate the dynamics of gas-liquid two-phase flow and made a noteworthy discovery. They observed that the Kelvin-Helmholtz (K-H) instability, driven by velocity gradients, gradually transitioned into the Rayleigh-Taylor (R-T) instability, governed by the forces of gravity and buoyancy, at the intersection interface of the two phases during the ejection process of the gaseous jets. Furthermore, through a combination of numerical simulation and experimental analysis, they discerned that the shape of the underwater gaseous jets comprised an airbag-like structure followed by a conical region. Under over-expanded conditions, the wake field exhibited remarkable instability, periodically manifesting expansion and necking phenomena. Wang et al. (2019) conducted numerical simulations employing Laval nozzle models featuring distinct expansion ratios. Their findings revealed that the morphology of the nozzle jet varied depending on the expansion ratio employed. Notably, nozzles with smaller expansion ratios exhibited a higher oscillation frequency, faster attenuation of working noise, and superior concealment, rendering them more suitable for underwater propulsion. He et al. (2015) performed numerical simulation on an annular throat conical plug operating at a Mach number of 2.0 within an over-expanded flow field. Their study revealed that the oscillation of the underwater gaseous jet flow field is primarily influenced by the gas-liquid two-phase interaction, which induces jet oscillation. Furthermore, they conducted numerical simulations on a floating mine under three distinct operational conditions. Xu et al. (2020) discovered that the occurrence of necking and fracture in the shell resulted in a reduction of resistance, while the bulging phenomenon significantly increased the resistance of the underwater vehicle. Additionally, under over-expanded conditions, the engine thrust exhibited an oscillation amplitude of 21.7%. Wu et al. (2018) simulated the gas flow dynamics within the nozzle and the formation of gas bubbles during the early stages of ignition. Their investigation revealed the establishment and subsequent destruction of shock waves during the initial phase. Furthermore, they observed a periodic compression-expansion phenomenon along the central axis of the gas jet during the flow process. Zhang (2019) conducted simulations on the initial ignition process of a rocket engine submerged in deep water. The study revealed a periodic oscillation in pressure, Mach number, and temperature at the outlet. Furthermore, it was observed that the pressure and velocity along the central axis of the nozzle remained constant once the jet reached a stable state.

Drawing upon the aforementioned studies, it can be inferred that the characteristic phenomena exhibited by underwater supersonic gaseous jets encompass bulging, necking, and back attack. (1) Bulging: As the gas is expelled, the presence of a vast aquatic environment diminishes its ability to displace water forcefully. Consequently, the contraction and expansion of shock waves generate a protruding bubble at the nozzle wall's exit, leading to an elevation in wall pressure. (2) Necking: Resulting from the compression of gas within the aquatic environment and the shear forces exerted by high-pressure reflux at the leading edge of the jet, the gas flow undergoes a constriction or fragmentation perpendicular to its trajectory. When the gas pressure at the constriction point falls below the external water pressure, the gas re-establishes supersonic gaseous jets through the narrowed section, causing the bubble to rupture. Conversely, if the gas pressure continues to rise and surpasses the external water pressure, the gas flow fails to form a supersonic jet through the constricted region, leading to an unbroken bubble that transforms into bulging. (3) Back attack: As the flow channel constricts, the airflow fracture bifurcates into two distinct streams. One stream proceeds downstream in alignment with the jet's direction, while the other stream impinges upon the nozzle and collides with the tail wall. The recurring interplay of bulging, necking, and back attack induces periodic fluctuations in pressure and thrust along the nozzle wall, thereby causing deviations in the navigation trajectory from its intended orbit. Consequently, the control of flow dynamics in underwater gaseous jets assumes paramount significance.

At present, most of the methods to suppress flow separation are applicable to the air environment. For example, Sreerag et al. (2021) adopted the method of secondary jet at the edge of the main nozzle to prevent air from entering the separation zone and eliminated the flow separation in the main nozzle. It was concluded that the secondary jet nozzle parallel to the main nozzle had the best effect. Emelyanov et al. (2022) numerically simulated supersonic gaseous jets in an extended nozzle. The external extension of the nozzle had an obvious effect on the flow distribution, and the formation of the separation zone had an adverse effect on the thrust. Cihan et al.

(2019) conducted drag reduction studies by applying the NACA 2415 airfoil vortex generator and front spoiler to the top of the minibus, and the results showed that both of these different structures can reduce the drag coefficient of the bus. Bayindirli & Celik (2023) applied a non-smooth surface plate to a minibus in a wind tunnel to study flow control, and the results showed that using a non-smooth surface plate in the front roof area of the minibus model could reduce the average drag coefficient by 1.03%. Passive control is mainly used to suppress flow separation by adding some small structures, such as vortex generators and spoilers, etc. The main mechanism is that the geometry of the structure brings high-speed fluid energy from the outside of the boundary layer into the boundary layer, which increases the ability of the boundary layer to overcome the inverse pressure gradient and delays the separation point of the flow boundary layer. Due to the intricate formation of a gas-liquid interface between swiftly moving gas and a water medium, the separation shear layer of underwater gaseous jets veers away from the wall, leading to the ingress of water into the reflux region. The interaction between these two phases becomes considerably intricate, and the airflow exerts an impact on the wall. Consequently, numerous research approaches, both domestic and international, prove unsuitable for the regulation of flow in underwater gaseous jets.

Porous media refers to a material comprising a solid phase and interconnected voids, which are dispersed either uniformly or unevenly within a given space. Porous media can be encountered in various aspects of our daily lives, such as soil, sponges, bread, and breakwaters. The presence of these voids renders the internal structure of porous media highly intricate, thereby endowing it with excellent wave attenuation characteristics. Consequently, porous media finds extensive application in coastal and marine engineering endeavors. As an illustration, Yu et al. (2014) conducted a comparative analysis between the simulation outcomes of a porous media model and a porous structure in terms of their influence on the flow characteristics surrounding rigid emergent vegetation. Utilizing numerical simulation techniques, their findings revealed that the porous structure exhibited favorable impacts on the turbulence properties and flow field structure in the vicinity of the columnar cluster. Moreover, employing a porous media model for large-scale flow calculations pertaining to vegetation demonstrated enhanced computational efficiency. Qiao et al. (2021) undertook flume experiments and numerical simulation to investigate the interplay between waves and a solitary permeable cylinder, as well as the composite configuration of a permeable cylinder encompassing a concentric inner cylinder. They scrutinized the influence of porosity and radius of the permeable cylinder on both the wave force exerted and the wave height within the permeable cylinder. Liu et al. (1999) introduced a computational model aimed at simulating the intricate interplay between waves and permeable structures. The outcomes of this study revealed a commendable concurrence between the numerical model's predictions for the permeable structure and the empirical data obtained from experiments. Lara et al. (2012) put forth an innovative IH-3VOF model, rooted in the VARANS equation and VOF methodology, to facilitate the simulation of two-phase flow within porous media. This model proves particularly valuable in scenarios where there exists a spatial gradient in porosity. The advent of this approach holds significant ramifications for the realm of coastal engineering, given the prevalence of coastal structures comprising diverse porosity configurations. Drawing from the aforementioned investigations, it becomes evident that porous media represents a highly viable and effective means of regulating fluid dynamics in liquid-dominated scenarios.

Drawing upon the aforementioned research context, this paper presents a novel application of a porous media layer to an underwater vehicle. Specifically, the porous media is strategically positioned along the tail wall of the nozzle to facilitate flow control. Subsequently, a comprehensive model of an underwater vehicle featuring porous media walls is constructed. Employing numerical calculation methods, this study scrutinizes various aspects, including the morphology of the jet, distribution of the tail flow field, variations in wall pressure, and magnitude of thrust. The findings derived from this research endeavor hold significant potential in offering valuable insights for further exploration into the stability performance of underwater vehicles.

2. MATHEMATICAL MODEL AND NUMERICAL METHOD

2.1 Model Equations

2.1.1 Control Equations

In the context of underwater supersonic gaseous jets, the governing equations employed encompass the conservation of mass, momentum, energy, and volume transport. These equations are formulated while taking into account factors such as buoyancy and surface tension, while disregarding any interphase mass and heat transfer. The mathematical expressions are as follows:

$$\frac{\partial \rho_m}{\partial t}+\frac{\partial\left(\rho_m u_i\right)}{\partial x}=0 \tag{1}$$

$$\frac{\partial\left(\rho_m u_i\right)}{\partial t}+\frac{\partial\left(\rho_m u_i u_j\right)}{\partial x}=-\frac{\partial p}{\partial x_i}+\frac{\partial}{\partial x_i}\left[\mu_m\left(\frac{\partial u_i}{\partial x_j}+\frac{\partial u_j}{\partial x_i}\right)\right]+S_i \tag{2}$$

$$\frac{\partial}{\partial t}\sum_{n=w,g}\left(\alpha_n \rho_n E_n\right)+\frac{\partial}{\partial x_j}u_j\sum_{n=w,g}\left[\alpha_n\left(\rho_n E_n+p\right)\right]=\frac{\partial}{\partial x_j}\left(k_{eff}\frac{\partial T}{\partial x_j}\right) \tag{3}$$

$$\frac{\partial}{\partial x_j}\left(\alpha_g \rho_g\right)+\frac{\partial}{\partial x_i}\left(\alpha_g \rho_g u_i\right)=0 \tag{4}$$

where, p is pressure, T *is* temperature, u_i and u_j are the velocity component, F_i is the source term, φ_m is the physical properties of the mixed phase, $\varphi_m=\varphi_g\alpha_g+\varphi_w(1-\alpha_g)$, φ_g and φ_w represent the gas phase density or viscosity coefficient, liquid phase density or viscosity coefficient; α_g and α_w represent the

gas phase volume fraction and liquid phase volume fraction, where $\alpha_g + \alpha_w = 1$.

2.1.2 Turbulence Model

In this paper, the Reynolds-averaged N-S equation is closed using the *k-ω* SST turbulence model, which combines the standard *k-ω* and *k-ε* models into one, activating the *k-ω* model for simulations in the near-wall surface region and using the *k-ε* model for solutions in the far field, with the following model equations:

$$\frac{\partial}{\partial t}(\rho k) + \frac{\partial}{\partial x_i}(\rho k u_i) = \frac{\partial}{\partial x_i}(\Gamma_k \frac{\partial k}{\partial x_i}) + G_k - Y_k + S_k \tag{5}$$

$$\frac{\partial}{\partial t}(\rho \omega) + \frac{\partial}{\partial x_i}(\Gamma_w \frac{\partial \omega}{\partial x_i}) + G_w - Y_w + D_w + S_w \tag{6}$$

where, *k* is turbulent kinetic energy, *ω is* turbulent dissipation rate, Γ is the effective diffusion coefficient, *G is the* production term, *Y is the* diffusion term, *D is the* cross-diffusion term , *S* is the user-defined source term.

2.1.3 VOF Model

The VOF model, employed to simulate the behavior of two or more immiscible fluids, relies on the utilization of momentum equations and phase volume fraction equations. These equations collectively govern the dynamics of the fluid system. During the computational process, the phase volume fraction variable is introduced to accurately track the interface between each computational unit. Specifically, for a given phase q, the equation governing the volume ratio can be expressed as follows

$$\frac{1}{\rho_q}\left[\frac{\partial}{\partial t}\left(\alpha_q \rho_q\right) + \nabla\left(\alpha_q \rho_q v_q\right)\right] = S_{\alpha_q} + \sum_{p=1}^{n}\left(\dot{m}_{pq} - \dot{m}_{qp}\right) \tag{7}$$

where, $\dot{m}_{pq}$ is the mass transfer from phase *q* to phase *p*, $\dot{m}_{qp}$ is the mass transfer from phase *p* to phase *q*. Typically, the source term at the right end of the equation is zero. The volume ratio of main phase is constrained by the following:

$$\sum_{q=1}^{n} \alpha_q = 1 \tag{8}$$

In this paper, the gas phase is an ideal compressible gas whose dynamic viscosity is 1.784×10^{-5} Pa•s, the liquid phase is water whose the density is 998.2 kg/m^3 and the dynamic viscosity is 1.003×10^{-3} Pa•s.

2.1.4 porous Model

Given the inherent complexity of porous structures, the simulation model is established employing the renowned commercial software, Ansys Fluent. Through this approach, a comprehensive calculation and analysis are carried out. The introduction of a porous media layer enables the simulation of resistance within the porous structure. By incorporating empirical assumptions, the flow resistance is incorporated into the designated region. In essence, this entails the addition of both inertial loss and viscous loss terms to the standard momentum equation:

$$S_i = -\left(\sum_{j=1}^{3} D_{ij}\mu v + \sum_{j=1}^{3} C_{ij}\frac{1}{2}\rho|v|v_j\right) \tag{9}$$

where S_i is the source term of the momentum equation, $|v|$ is the velocity, *D* is the viscous resistance coefficient matrix, *C* is the inertial resistance coefficient matrix, μ is the liquid viscosity coefficient, and ρ is the liquid density.

For isotropic porous media, equation (3) can be simplified as:

$$S_i = -\left(\frac{\mu}{\alpha}v_i + C_2\frac{1}{2}\rho|v|v_j\right) \tag{10}$$

where $\frac{1}{\alpha}$ is the viscous resistance coefficient and C_2 is the inertial resistance coefficient.

2.1.5 Solving Methods

In this paper, the finite volume method was used to discrete the control equation, and the Simple algorithm of the separation solver and the pressure coupled equations was used to solve the control equation. The Body-Force-Weight algorithm was used to solve the pressure solution, and the Geo-Reconstruct scheme was used for the volume fraction equation. The energy equation and the momentum equation were discretized by the second-order upwind scheme. All of the simulations were modeled using the commercial CFD (Computational Fluid Dynamics) code, ANSYS Fluent®.

2.2 Geometric Model and Calculation of Working Conditions

2.2.1 Computational Model and Boundary Conditions

This paper employs a two-dimensional axisymmetric model to computationally investigate the impact of a porous media layer on the behavior of underwater supersonic gaseous jets emitted by an underwater vehicle. The computational domain is shown in Fig. 1, where the simulated water depth is 200m, the pressure of the gas

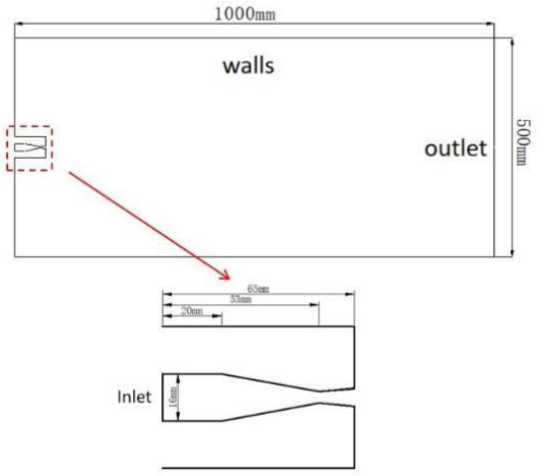

Fig. 1 Calculation domain and boundary conditions

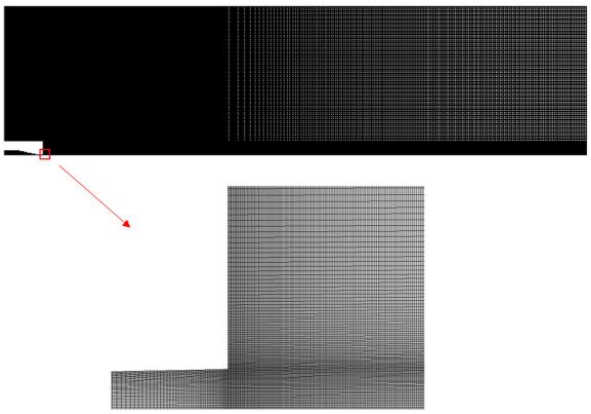

Fig. 2 Computational mesh

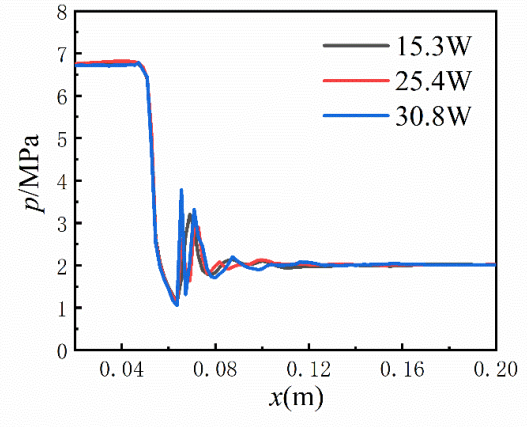

Fig. 3 Mesh independent study

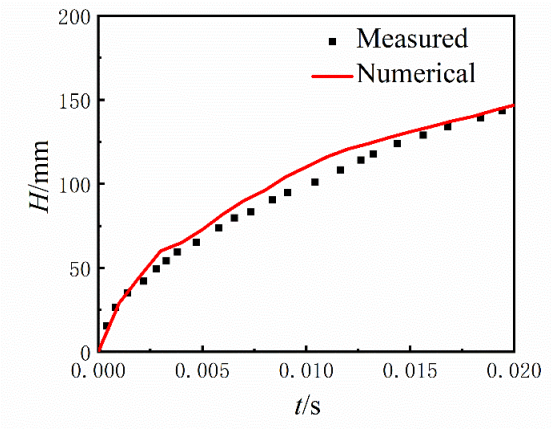

Fig. 4 Comparison between experiment and simulation results of jet height

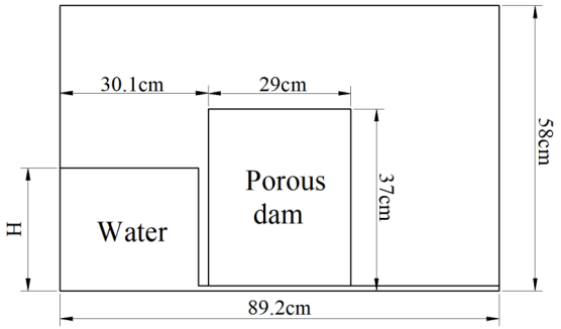

Fig. 5 Setup of porous dam breaking (1)

inlet is 6.7 MPa and the pressure of ambient water is set to 2.0 MPa, and the remaining boundary conditions are set to no-slip walls. Using the water ambient pressure for the initialization of the calculation domain, the compressible gas is in the nozzle area, and the pressure is 4 MPa when the cover was opened. The entirety of the computational domain employs structured meshing, owing to the presence of high-speed flow within the nozzle tail. To guarantee the precision of the calculation outcomes, refinement is implemented in the nozzle throat, wall, and external flow field region at the nozzle outlet. The computational meshes utilized are depicted in Fig. 2. In order to exclude the influence of the meshes on the calculation results, different densities of meshes are used (15.3w, 25.4w and 30.8w) for mesh-independent verification, respectively. Figure 3 illustrates the various mesh conditions employed to calculate the axial pressure distribution of the jet. Notably, the calculation results obtained using meshes of 15.3w and 25.4w exhibit a relative error of 5.3%, while the results obtained using meshes of 25.4w and 30.8w display a relative error of 2.1%. Consequently, the mesh configuration of 25.4w was ultimately selected for the following numerical simulation study.

3. VALIDATION

To verify the precision of the numerical approach employed in this paper, numerical simulations were conducted under identical operating conditions as the underwater gaseous jet experiments documented in literature. Subsequently, a comparison was made between the numerical simulation results and the experimental findings. Figure 4 illustrates temporal evolution of the gas height of the jet, as derived from both experimental data and numerical simulations. The outcomes demonstrate a commendable concurrence between the numerical simulation outcomes and the experimental data, thereby affirming the viability of the numerical simulation methodology employed in this study for investigating the flow control characteristics of underwater gas jet flow through the application of porous media layers.

Prior to employing the porous media model, it is imperative to validate the accuracy of the model itself. This can be accomplished by leveraging the experimental findings of Liu et al. (1999) and Billstein et al. (1999) regarding the failure of porous media dams. In the experiment conducted by Liu, a meticulously constructed high-level water reservoir and an artfully fashioned porous dam were employed. The outflow of water from the reservoir was deftly regulated through the use of a gate. The porous dam itself was comprised of gravel, boasting an average diameter of 1.59 cm and a porosity of 0.49. The alternative configuration entailed the utilization of glass beads, characterized by an average diameter of 0.3 cm and a porosity of 0.39. On the left side, the water depth height H was measured at 24 cm and 14 cm, respectively. The spatial extent of the computational domain for the numerical simulation is depicted in Fig. 5. Within the

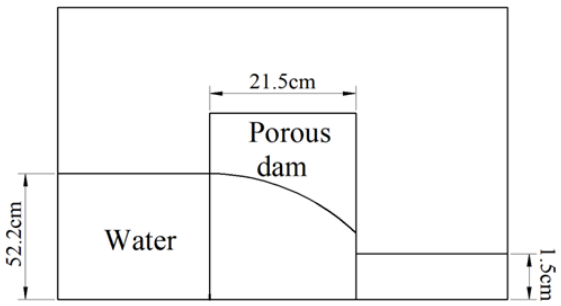

Fig. 6 Setup of porous dam breaking (2)

realm of the Billstein experiment, the porous dam spanned a length of 21.5 cm, while the left water depth reached a towering 52.2 cm, juxtaposed with a mere 1.5 cm on the right side. The porous dam employed in these experiments was meticulously crafted using spherical glass beads, boasting an average diameter of 0.2 cm and a porosity of 0.34. The visual representation of the computational domain can be observed in Fig. 6.

Figures7 and 8 present a juxtaposition of the numerical simulation outcomes with the experimental findings of Liu. This comparative analysis unveils that the disparity observed in the calculated value of the initial free surface opening of the water gates during the experiment, which ensued with a swift 0.1s duration. Consequently, the water situated at the lowermost region initiated its motion prior to the water in proximity to the free surface. Figure 9 illustrates the numerical simulation outcomes in contrast to Billstein's experimental results. In general, the numerical simulation results exhibit commendable concurrence with the experimental results across all three porous media. Therefore, as shown in Fig. 10, three different porous media layers are designed in this paper, the shape of which is a ring column with a thickness of 2mm. The porosity of the porous medium layer is 0.34, 0.39 and 0.49, respectively. The porous media layer is located on the wall layer near the nozzle outlet.

4. RESULTS AND DISCUSSION

4.1 Quantitative Analysis of Wake Flow Field Parameters

In this paper, the wall region at the nozzle outlet designated as a layer of porous media to investigate its impact on controlling the stability of the tail flow field. Since there is a dearth of literature exploring the utilization of porous media for regulating flow field parameters at the nozzle's tail, this study delves into the realm of porous media research primarily focused on physical model experiments pertaining to breakwaters. Therefore, this paper employs three distinct porosity values (n=0.34, n=0.39, n=0.49) validated in Section 3, in order to simulate and analyze the influence of varying porosity on

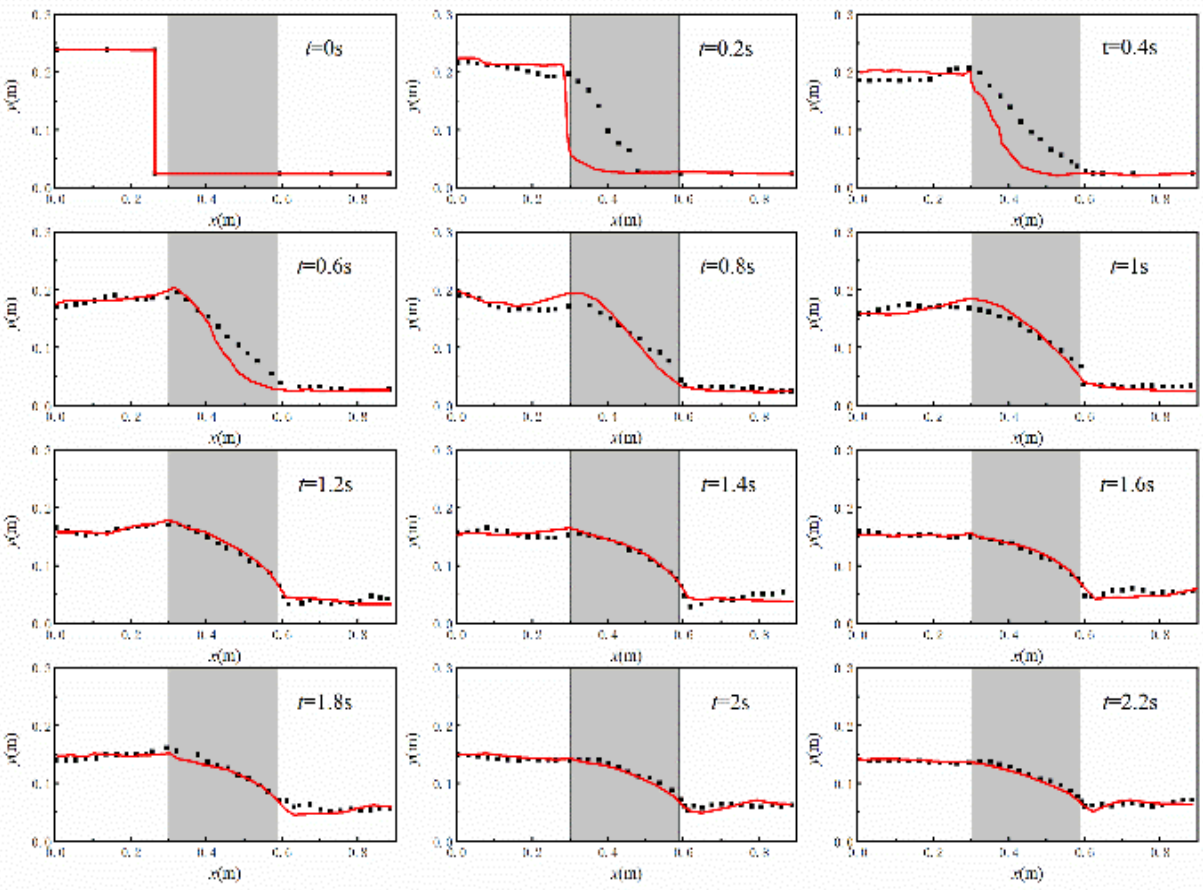

Fig. 7 Comparison of experimental data (square) and numerical results (red curves) of water surface elevation at *n*=0.49

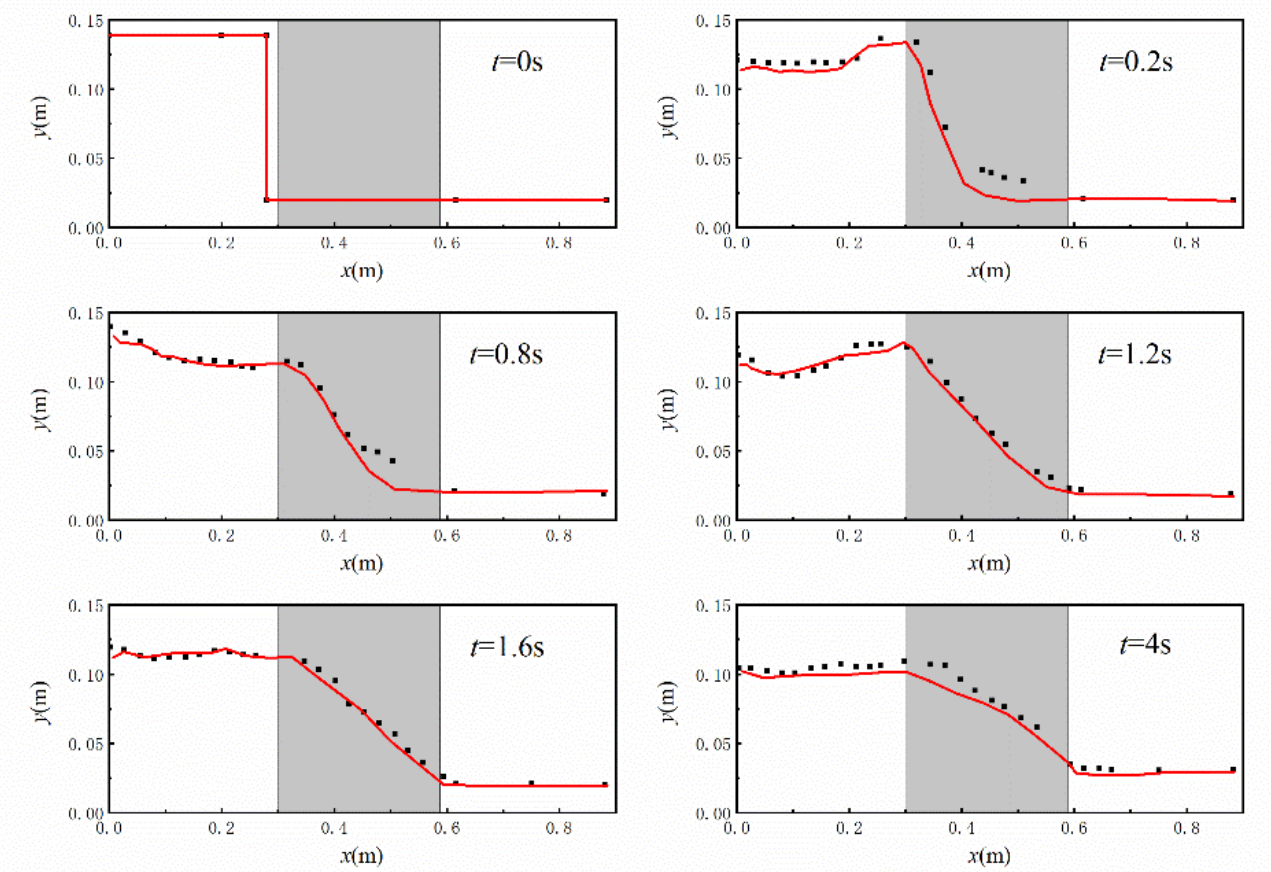

Fig. 8 Comparison of experimental data (square) and numerical results (red curves) of water surface elevation at *n*=0.39

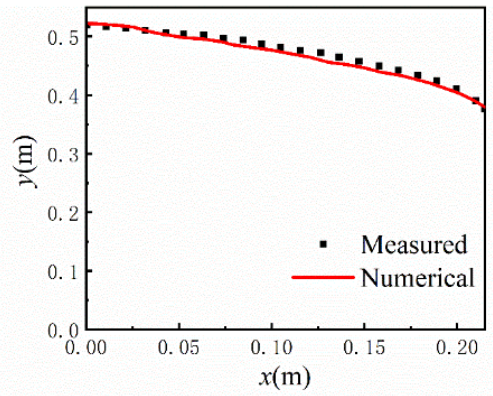

Fig. 9 Comparison of experimental data (square) and numerical results (red curves) of water surface elevation at *n*=0.34

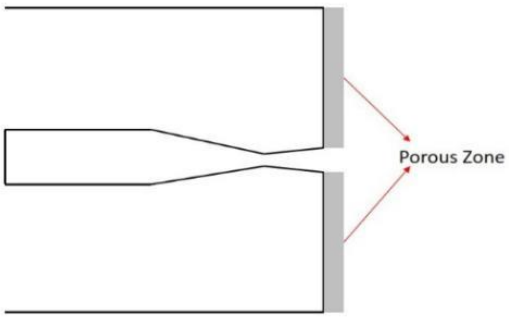

Fig. 10 Schematic diagram of the porous media model

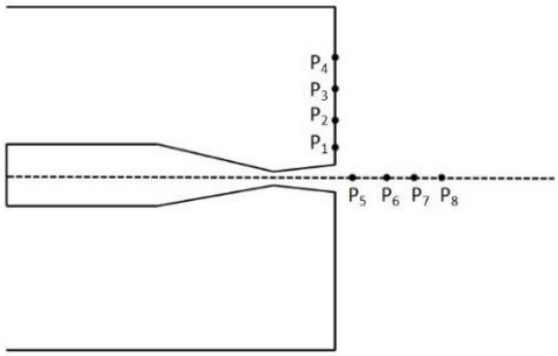

Fig. 11 Diagram of pressure monitoring points

during the dam breach can be attributed to the manual mitigating wall pressure pulsations. The pressure monitoring points set up in this paper are shown in Fig.11. Among these, P_1 - P_4 is the monitoring point on the wall, the position distribution from the nozzle outlet is d_e, $3d_e$, $5d_e$ and $7d_e$, and P_5 - P_8 is the monitoring point on the axis, and the distance from the nozzle outlet is d_e, $3d_e$, $5d_e$ and $7d_e$, respectively.

In order to assess the suppression effect of porous media under different parameters more intuitively and conveniently, this paper uses the pressure fluctuation rate as the main evaluation parameter, which is defined as the value of pressure fluctuation as a percentage of the ambient

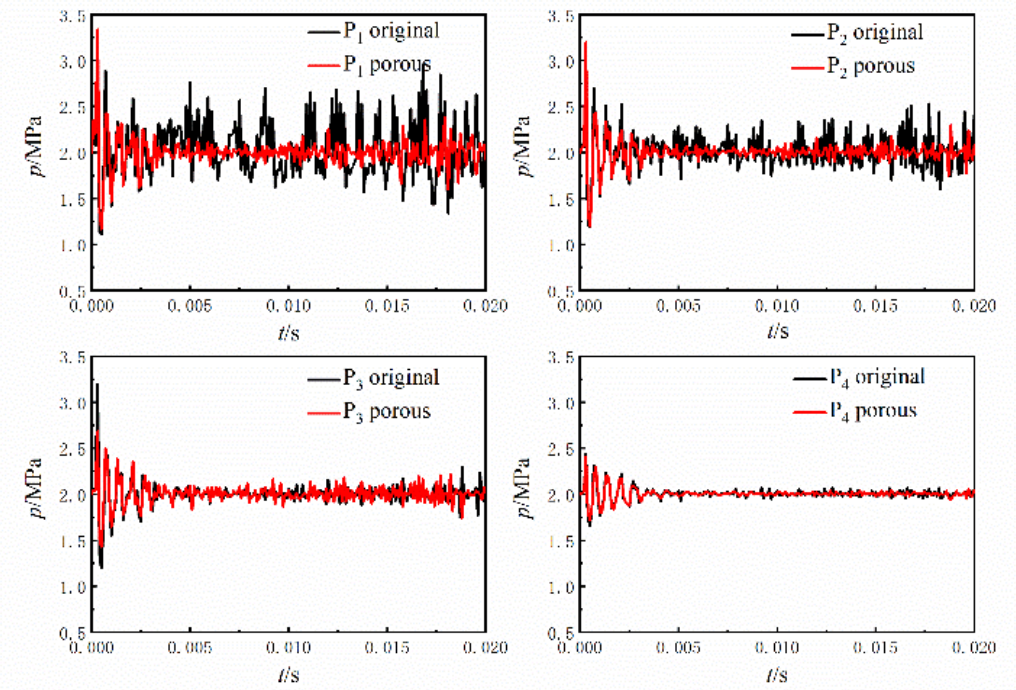

Fig. 12 When *n*=0.34, pressure value at the monitoring point of the tail wall compared to the wall without porous media

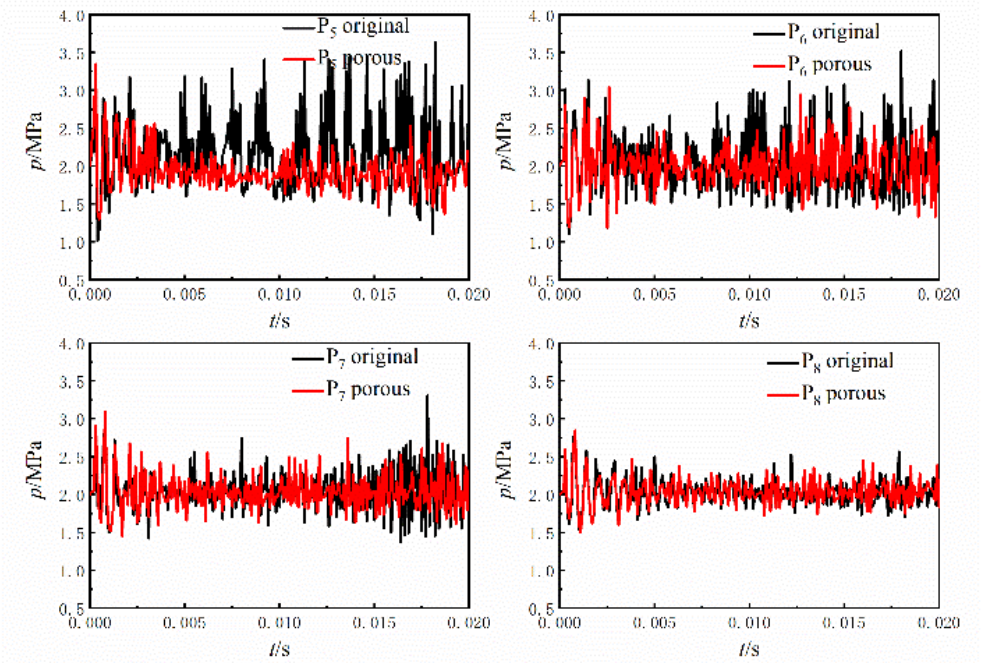

Fig. 13 When *n*=0.34, axial monitoring point pressure values compared to walls without porous media

pressure value, and the pressure fluctuation rate R is defined by the following formula:

$$R = \left| \frac{\psi_N - \psi_A}{\psi_A} \right| \tag{11}$$

where, ψ_N is the pressure value of the monitoring point, ψ_A is the pressure value of the external ambient water. From the equation, the smaller the R-value indicates the smaller the amplitude of the pressure fluctuation, indicating a better suppression effect of the porous media.

Figures 12-17 depict the pressure values at the monitoring points along the tail wall, as well as the axial monitoring points, in comparison to the wall devoid of porous media, exhibiting various porosity levels. These figures vividly demonstrate that all three types of porous media layers with distinct porosity values exert a control effect on pressure fluctuation, with *n*=0.34 showcasing the most pronounced efficacy. Observing Fig. 12, Fig. 14 and Fig. 16, it becomes evident that as one approaches the nozzle outlet, the amplitude of pressure oscillation at the wall intensifies. Without porous media, the pressure at P_1 produced a larger oscillation with a major oscillation

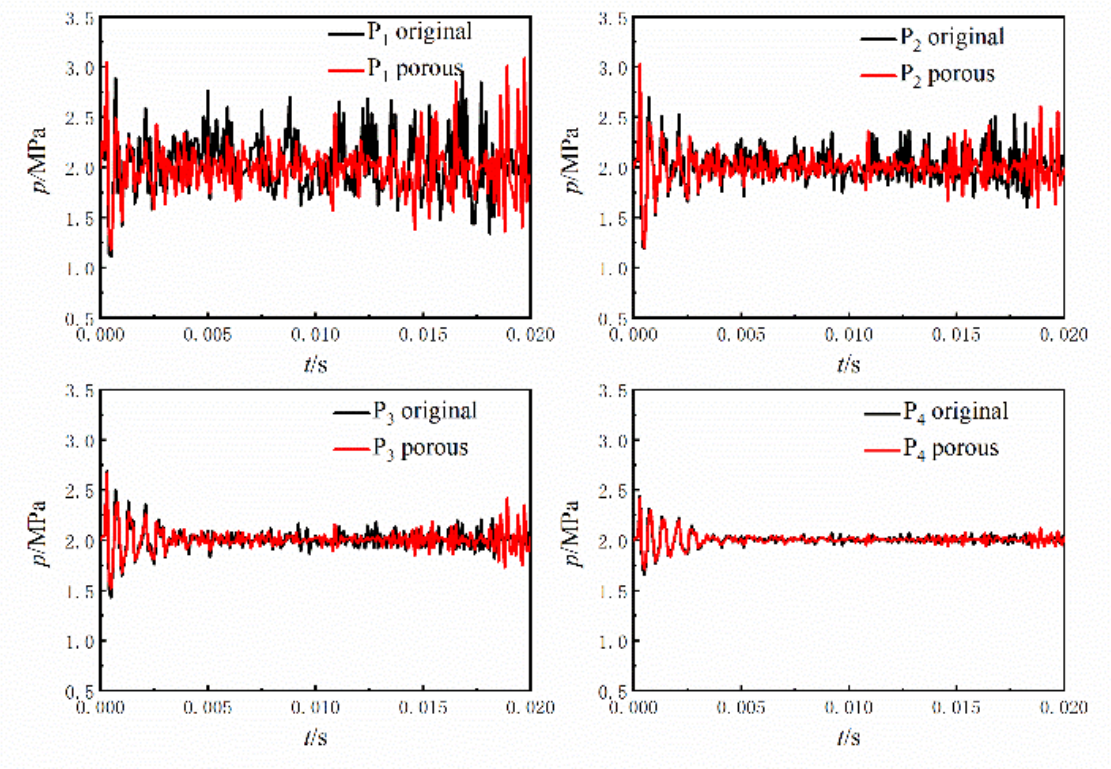

Fig. 14 When *n*=0.39, pressure value at the monitoring point of the tail wall compared to the wall without porous media

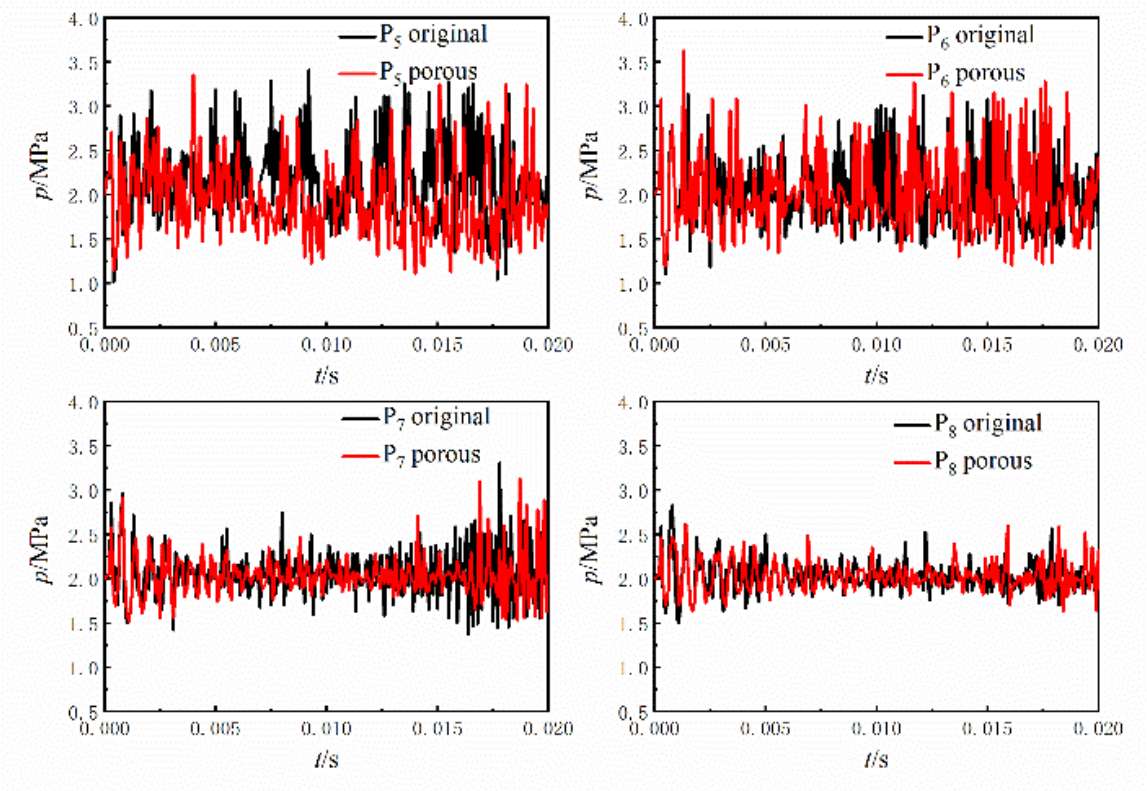

Fig. 15 When *n*=0.39, axial monitoring point pressure values compared to walls without porous media

range of 1.5-3 MPa; after the addition of porous media, the pressure oscillation range is 1.7-2.2 MPa, with the exception of the initial stage. Figure 13, Fig.15 and Fig.17 illustrate the pressure distribution at the axial monitoring point revealing that proximity to the nozzle outlet yields optimal suppression of pressure pulsation, owing to the presence of porous media. Upon comparing the three distinct porous media samples with varying porosity levels, it is discerned that a porosity value of 0.34 yields the most favorable outcome. Consequently, for the

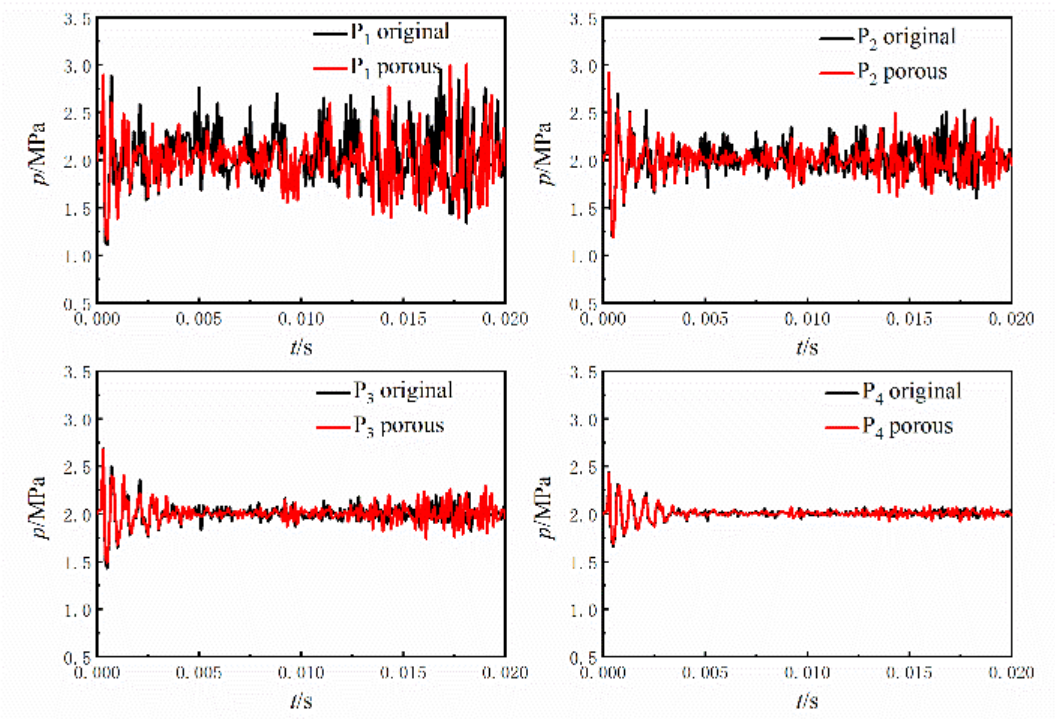

Fig. 16 When *n*=0.49, pressure value at the monitoring point of the tail wall compared to the wall without porous media

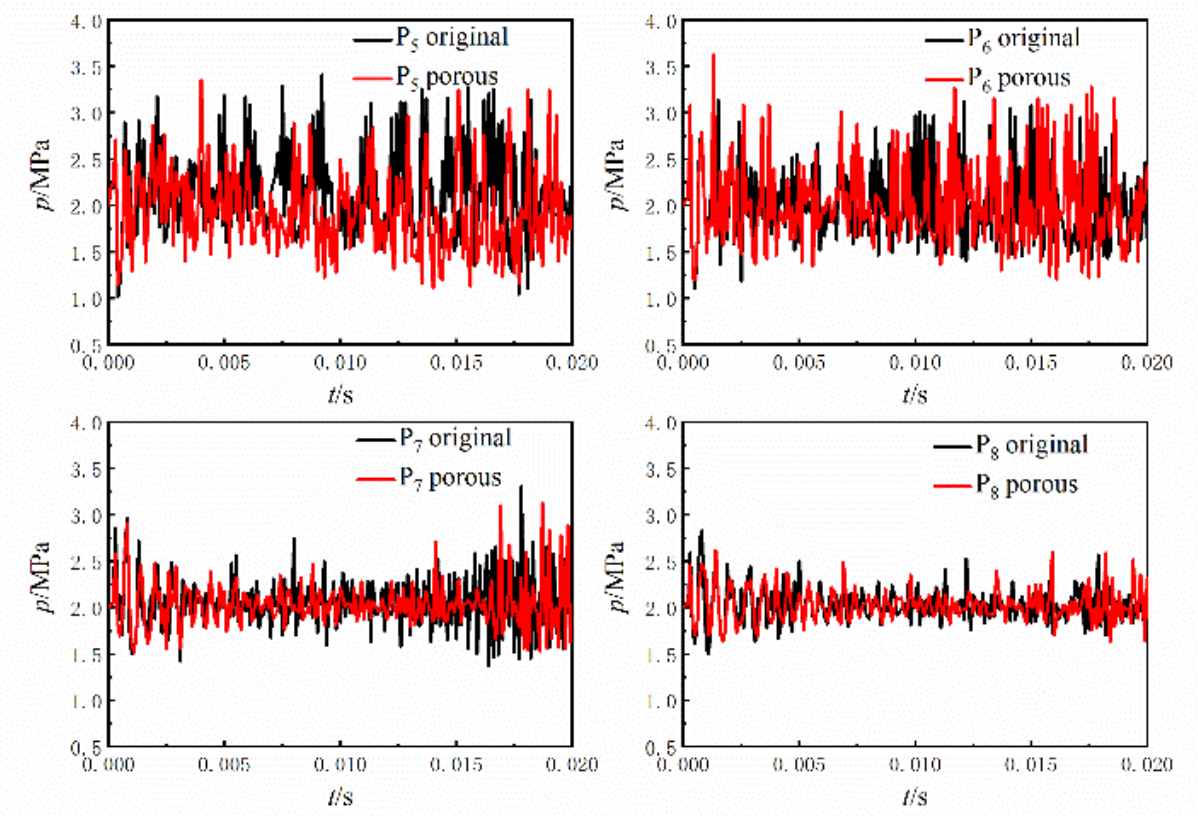

Fig. 17 When *n*=0.49, axial monitoring point pressure values compared to walls without porous media

purpose of comparison, the pressure fluctuation rate R_1 is computed without the presence of porous media, while the pressure fluctuation rate R_2 is calculated specifically for a porosity of 0.34. The ensuing results are visually presented in Fig.18 and Fig. 19.

Figures 18 and 19 present the temporal evolution of pressure fluctuation rates at the nozzle outlet wall and the axial monitoring point, respectively, for a porosity of *n*=0.34. Examining Fig.18, it becomes apparent that the initial pressure oscillation at the nozzle's tail wall is rather

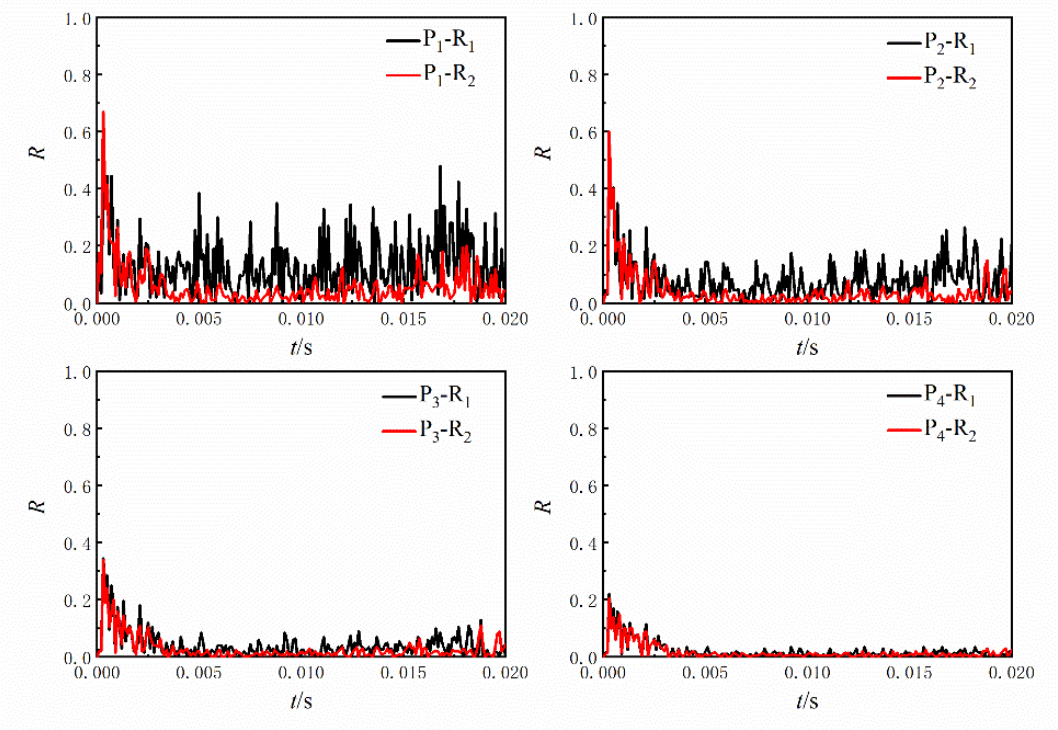

Fig. 18 When *n*=0.34, comparison of R-values at tail wall monitoring points

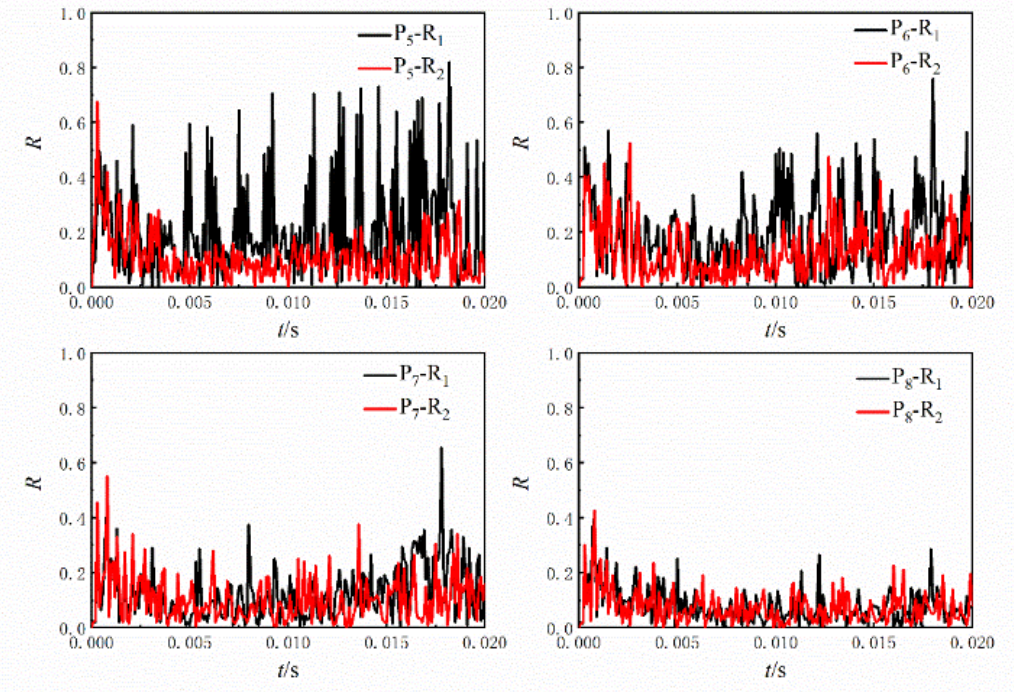

Fig. 19 When *n*=0.34, comparison of R-values for axial monitoring points

vigorous, resulting in a pressure fluctuation rate of R_1 of 0.4 at point P_1. As the tail flow field further develops, the pressure at the wall attains a stable oscillatory state with a pulsation rate of approximately 0.2. Notably, the proximity to the nozzle corresponds to an amplified value of the pressure fluctuation rate. After the tail wall surface has n = 0.34 porous media, except for the initial stage, the pressure pulsation rate at P_1 fluctuates above and below 0.05. In Fig.19, it can be seen that at the distance of d_e from the nozzle outlet, P_5 monitoring point pressure oscillation amplitude is more violent, the pressure pulsation rate is about 0.8. Besides, when the porous media is set n=0.34 at the tail wall, the pressure fluctuation rate drops to about 0.2. According to the above analysis, the porous media with n=0.34 is used to further analyze the mechanism of pressure pulsation suppression by the porous media.

4.2 Analysis of Typical Processes in Underwater Gaseous Jets

The development of underwater gaseous jets can be categorized into three main stages: bulging, necking, and

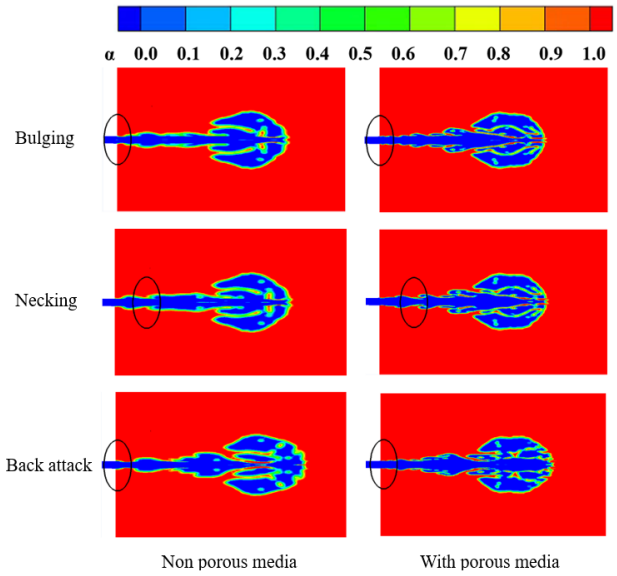

Fig.20 Comparison of different stages in typical process of underwater gaseous jets

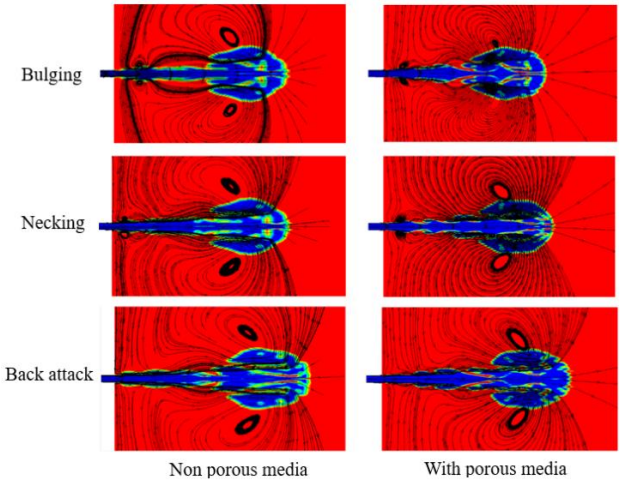

Fig. 21 Comparison of streamline diagrams in various stages of typical process of underwater gaseous jets

back attack. Figure 20 and Fig. 21 reveal that during the bulging stage, the presence of porous media partially suppresses the bulging phenomenon of the airbag near the wall, consequently reducing the volume of bulging bubbles. In the necking stage, the necking position typically occurs at a considerable distance from the nozzle outlet, thereby rendering porous media ineffective in this stage. As for the back attack stage, the pressure exerted by the surrounding water environment causes some airflow to flow forward after the necking fracture, resulting in a back attack phenomenon. However, due to the existence of porous media, the airflow directed back towards the wall is noticeably attenuated.

To delve deeper into the quantitative analysis of jet morphology characteristics and their patterns of variation, this study introduces the notions of jet width and height. The jet height, denoted as H, represents the vertical distance from the tail wall of the nozzle to the highest point of the gas-water interface. On the other hand, the jet

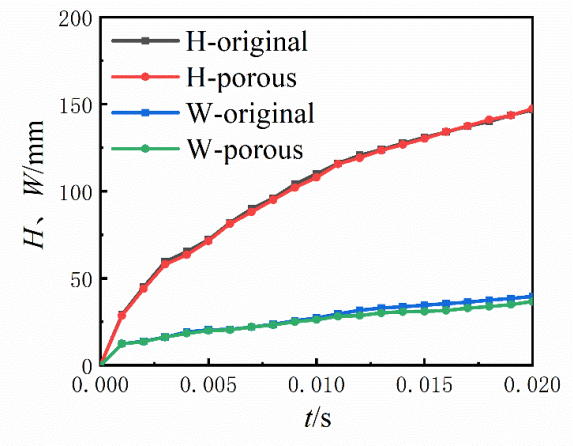

Fig. 22 Comparison of jet height and width

width, denoted as W, encompasses the span from the leftmost gas-water interface to the rightmost gas-water interface. Figure 22 illustrates the evolution of jet height and width for both non-porous and porous media. Notably, the variation of jet height over time follows a relatively regular pattern, characterized by a swift initial increase in jet height followed by a more gradual ascent. This phenomenon primarily stems from the initial stage of the jet, wherein the momentum remains substantial and is relatively unaffected by the surrounding water environment. As the gas continues to be expelled, the jet velocity becomes less influenced by the water environment, resulting in a gradual increase in both height and width as the entire air column becomes constrained. Notably, the presence of porous media at the nozzle outlet wall exhibits negligible impact on the height and width of the gas jet. Consequently, it can be inferred that porous media also exerts minimal influence on the overall morphology characteristics of the gas jet.

4.3 Analysis of Oscillations in the Wake Flow Field Parameters

In order to delve deeper into the evolution of tail wall pressure throughout the three distinctive stages of gaseous jets - bulging, necking, and back attack - influenced by porous media, the contour with an iso-volume of 0.8 for the gas is selected for analysis, as depicted in Figs. 23-25. From the data, it is evident that: (1) During the expansion phase, the airbag's capacity to displace external water is feeble, resulting in the formation of a high-pressure region near the boundary. However, when a porous medium is present at the boundary, the extent of this high-pressure region near the nozzle outlet, caused by the expansion, is diminished. This can be primarily attributed to the fact that as water traverses through the porous medium, the pressure exerted on the boundary surface is reduced due to the resistance encountered during flow. Consequently, this reduction in pressure leads to a decrease in the compression level of the air bladder bubble and subsequently reduces the area encompassing high pressure. (2) During the necking phase, a substantial pressure disparity between the interior and exterior of the bubble ensues, resulting in the contraction of the gas-liquid interface towards the center, thus giving rise to a region of heightened pressure at the narrowing point. By

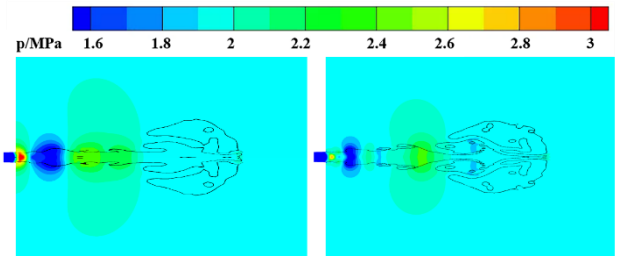

Fig. 23 Comparison of pressure in the bulging stage between non porous media and porous media on the tail wall

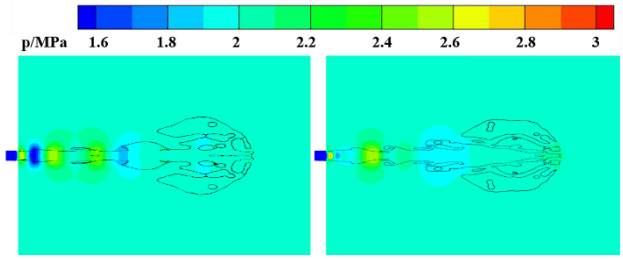

Fig. 24 Comparison of pressure in the necking stage between non porous media and porous media on the tail wall

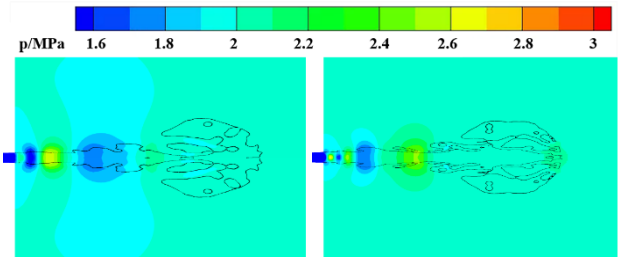

Fig. 25 Comparison of pressure in the back attack stage between non porous media and porous media on the tail wall

examining the illustration, it becomes apparent that the presence of porous media has minimal impact on this particular area, as the necking position is distant from the nozzle outlet, thereby precluding any significant alteration in wall pressure. (3) During the rearward thrust phase, the gas exhibiting a negative velocity generates a region of reduced pressure in close proximity to the nozzle wall. However, the presence of a porous media layer on the wall curtails the extent of this low-pressure zone. This phenomenon arises from the dissipation of momentum as the airflow traverses through the porous media, thereby diminishing the intensity of the rearward thrust exerted on the wall. In essence, as the underwater gaseous jets undergo transformations throughout different stages of jet formation, they not only impact the internal characteristics of the bubble but also induce pressure oscillations within the downstream flow field, consequently influencing the engine's operational performance. Nonetheless, when a porous media is present on the tail wall, it not only restrains the amplitude of pressure fluctuations in the downstream flow field to some extent but also exerts minimal influence on the jet structure. Hence, it can be inferred that the incorporation of porous media can enhance the engine's operational performance to a certain degree.

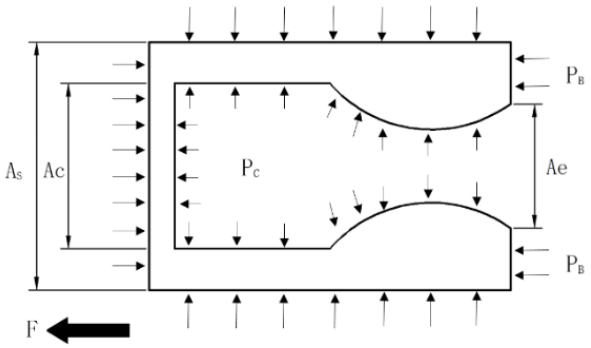

Fig. 26 Schematic diagram of the forces on the underwater engine

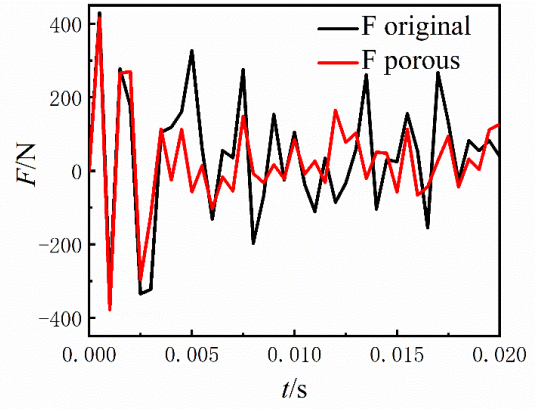

Fig. 27 Comparison of total thrust

4.4 Thrust Magnitude Analysis

The propulsion of the nozzle is depicted in Fig.26. The methodology employed for calculating the thrust of an underwater vehicle differs slightly from that of an air-based engine due to the influence of the surrounding water pressure. In the underwater environment, the static pressure exerted on the rear of the vehicle does not equate to the ambient pressure. Consequently, an additional term arises, referred to as pressure thrust, which accounts for the disparity between these two pressures. Thus, the total thrust F generated by the underwater vehicle can be expressed as the summation of the gas thrust F_1 and the thrust F_2 arising from the pressure differential between the front and rear surfaces.

$$F_1 = \dot{m}v_e + (p_e - p_h)A_e \tag{12}$$

$$F_2 = (p_B - p_h)(A_s - A_e) \tag{13}$$

$$F = \dot{m}v_e + (p_e - p_h)A_e + (p_B - p_h)(A_s - A_e) \tag{14}$$

where $\dot{m}$ is the gas mass flow, v_e is the nozzle out velocity, p_e is the out static pressure, A_e is the outlet area, p_h is the water environment pressure, and A_s is the tail wall area.

To delve deeper into the impact of porous media, possessing a porosity of 0.34， on the propulsive force produced by the nozzle, a comparative analysis is conducted between the nozzle thrust in the absence and presence of such media. As depicted in Fig. 27, it becomes evident that the nozzle thrust undergoes vigorous oscillations

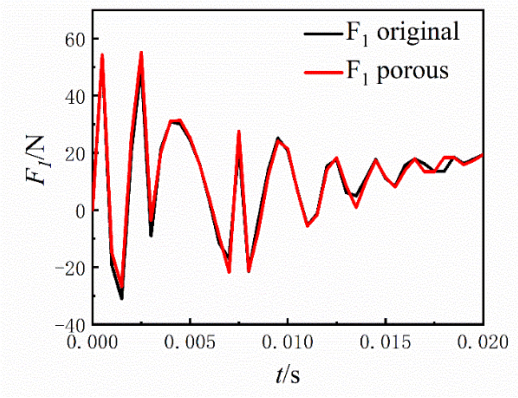

Fig. 28 Comparison of the thrust generated by gas

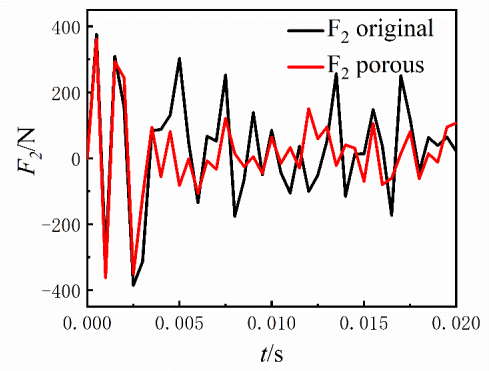

Fig. 29 Comparison of differential pressure thrusts

during its initial phase, accompanied by the emergence of negative thrust. This is primarily attributed to the occurrence of various phenomena, such as bulging, necking, and back attack, in the wake field of the underwater vehicle near the nozzle under over-expanded conditions. Consequently, the outlet pressure of the nozzle experiences violent pulsations, giving rise to periodic oscillations in thrust. During the initial stage, the instantaneous ejection of the jet and the pressure impact from the surrounding water medium result in intense thrust oscillations, leading to a relatively significant peak in initial thrust. At this juncture, due to the low pressure within the nozzle, there is a "backflow" of the external water medium into the interior of the nozzle, thus giving rise to the phenomenon of negative thrust. As the gas jet gradually stabilizes, the thrust also progressively settles into a state of steady oscillation. The diagram illustrates that after the addition of porous media to the tail wall, the nozzle also produces oscillating thrust, while the amplitude of oscillation decreases to a certain extent after the jet state tends to be stable. In order to further analyze the causes of this process, the thrust generated by the nozzle is divided into two parts, one is the thrust F_1 generated by gas, and the other is the thrust F_2 generated by differential pressure, as shown in figs. 28 -29. The illustration reveals that the permeable substance scarcely impacts the propulsion F_1 engendered by the gas. Once the jet state gravitates towards stability, the magnitude of F_1 oscillates around 18N However, the permeable substance significantly affects the thrust F_2 which is a result of the differential pressure. The presence of porous media attenuates the amplitude of pressure fluctuations on the tail wall, leading to a decrease in the amplitude of the differential pressure thrust oscillation produced by the nozzle. Consequently, the oscillation amplitude of the total thrust generated by the nozzle is diminished, enhancing the stability of the engine.

5. CONCLUSION

This manuscript delves into the issue of fluctuating propulsion produced by subaqueous vehicles under over-expanded circumstances, and introduces a novel methodology to manipulate its gaseous jet configuration by incorporating a porous media layer on the nozzle's rear wall. This concept is derived from the analogous flow control observed in submarine coral reefs and breakwaters that exhibit similar porous media structures. Computational simulations of the nozzle's gaseous jets, supplemented with porous media on the tail wall, are executed, and the influence of the porous media model on the gaseous jet configuration and engine efficiency is scrutinized， leading to the following conclusions:

(1) In view of the three typical phenomena of bulging, necking and back attack caused by underwater supersonic gaseous jets under over-expanded conditions, the bulging and back attack phenomenon can be significantly reduced by adding a porous medium layer at the tail of the nozzle.

(2) The porous media layers with porosity of 0.34, 0.39, and 0.49 have a certain flow control effect on underwater gas jets, among which the porous media layer with porosity of 0.34 has the best effect. The installation of porous media layer on the tail wall can suppress the oscillation of wall pressure when the gas flow bulges and returns.

(3) The porous media has almost no effect on the thrust F_1 generated by the engine, but has a greater impact on the thrust F_2 generated by the pressure difference effect. The porous media with porosity of 0.34 has a good control effect on the oscillations of the differential pressure thrust generated by the engine, thus controlling the oscillations of the total thrust generated by the nozzle and thus improving the stability of the underwater vehicle.

REFERENCES

Bayindirli, C., & Celik, M. (2023). Experimental optimization of aerodynamic drag coefficient of a minibus model with non-smooth surface plate application. *Journal of Engineering Studies and Research*, *28*(4), 34-40. https://doi.org/10.29081/jesr.v28i4.004

Cihan, B. (2019). Numerical drag reduction of a ground vehicle by NACA2415 airfoil structured vortex generator and spoiler. *International Journal of Automotive Technology 20,* 943–948. https://doi.org/10.1007/s12239-019-0088-6

Emelyanov, V., Volkov, K., & Yakovchuk, M. (2022). Unsteady flow simulation of compressible turbulent flow in dual-bell nozzle with movement of extendible section form its initial to working position. *Acta*

Astronautica, *194*, 514-523. https://doi.org/10.1016/j.actaastro.2021.10.007

Fluent, A. (2011). Ansys fluent theory guide. Ansys Inc., USA.

Fronzeo, M., & Kinzel, M. (2016). *An investigation of gas jets submerged in water*. Proceedings of the 46th AIAA Fluid Dynamics Conference. Washington, DC, US: AIAA, 1-17. https://doi.org/10.2514/6.2016-4253

Gong, Z. X., Lu, C. J., Li, J., & Cao, J. Y. (2017). The gas jet behavior in submerged Laval nozzle flow. *Journal of Hydrodynamics*, *29*(6), 1035-1043. https://doi.org/10.1016/S1001-6058(16)60817-X

He, M. S., Tan, L. L., & Liu, Y. (2015). Numerical investigation of flow separation in an annular conical aerospike nozzle for underwater propulsion. *Journal of Propulsion Technology*, *36*(1), 37-46. https://doi.org/10.13675/j.cnki.tjjs.2015.01.006

Lara, J. L., Jesus, M. D., & Losada, I. J. (2012). Three-dimensional interaction of waves and porous coastal structures Part II: Experimental validation. *Coastal Engineering*, *64*, 26-46. https://doi.org/10.1016/j.coastaleng.2012.01.009

Li, T. T., Hu, J., Cao, X. J., & Yu, Y. (2017). Underwater gas jet clamping process of annular nozzle. *CIESC Journal*, *68*(12), 4565-4575. https://doi.org/10.11949/j.issn.0438-1157.20170666

Liu, L. F., Lin, P., Chang, K. A., & Sakakiyama, T. (1999). Numerical modeling of wave interaction with porous structures. *Journal of Waterway, Port, Coastal, and Ocean Engineering*, *125*(6), 322-330. https://doi.org/10.1061/(ASCE)0733-950X(1999)125:6(322)

Loth, E., & Faeth, G. M. (1989). Structure of underexpanded round air jets submerged in water. *International Journal of Multiphase Flow*, *15*(4), 589-603. https://doi.org/10.1016/0301-9322(89)90055-4

Billstein, M., Svensson U. & Johansson N. (1999) Development and validation of a numerical model of flow through embankment dams – comparisons with experimental data and analytical solutions. *Transport in Porous Media*, *35*(3), 395-406. https://doi.org/10.1023/A:1006531729446

Qiao, D. S., Mackay, E., Yan, J., Yan, J., Feng, C. L., & Li, B. B. (2021). Numerical simulation with a macroscopic CFD method and experimental analysis of wave interaction with fixed porous cylinder structures. *Marine Structures*, *80*, 103096-103110. https://doi.org/10.1016/j.marstruc.2021.103096

Shi, H. H., Wang, B. Y., & Dai, Z. Q. (2010). Research on the mechanics of underwater supersonic gas jets. *Science China Physics, Mechanics & Astronomy*, *53*, 527-535. https://doi.org/10.1007/s11433-010-0150-x

Sreerag, V. N., Mohammad, F., Nandan, V., & Pramod, A. (2021). Parametric study on a method to control flow separation in rocket nozzles. *Materials Today: Proceedings*, *46*(19), 9950-9955. https://doi.org/10.1016/j.matpr.2021.03.291

Tang, J. N., Wang, N. F., & Shyy, W. (2011). Flow structures of gaseous jets injected into water for underwater propulsion. *Acta Mechanica Sinica*, *27*(4), 461-472. https://doi.org/10.1016/j.oceaneng.2020.107611

Tang, Y. L., Li, S. P., Liu, Z., Sui, X., & Wang, N. F. (2016). Research on thrust fluctuation characteristics of underwater solid rocket motor. *Journal of Solid Rocket Technology*, *39*(4), 476-481. https://doi.org/10.7673/j.issn.1006-2793.2016.04.005

Wang, L. L., Liu, Y., Li. D. Q., Wu, Q., & Wang, G. Y. (2019). Numerical study on underwater supersonic jet of solid rocket engine. *Acta Armamentarii*, *40*(6), 1161-1170. https://doi.org/10.3969/j.issn.1000-1093.2019.06.006

Wu, Y., Li, Z., & Jiang, X. R. (2018). Numerical analysis for underwater ignition two-phase flow field of solid rocket motor. *Journal of Aerospace Power*, *33*(10), 2508-2514. https://doi.org/10.13224/j.cnki.jasp.2018.10.024

Xu, H. Y., Luo, K., Liu, F. Q., Zuo, Z. H., Gu, J. X., & Huang, C. (2020). Effects of underwater supersonic jet on force characteristics of floating mine. *Journal of Propulsion Technology*, *41*(11), 2623-2629. https://doi.org/10.13675/j.cnki.tjjs.200397

Yu, L. H., Zhan, J. M., & Li, Y. S. (2014). Numerical simulation of flow through circular array of cylinders using multi-body and porous models. *Coastal Engineering Journal*, *56*(3), 1450014-1450040. https://doi.org/10.1142/S0578563414500144

Zhang, L. (2019). Numerical simulation of tail flow field for underwater solid rocket motor. *Journal of Solid Rocket Technology*, *42*(2),159-163. https://doi.org/10.7673/j.issn.1006-2793.2019.02.004

Zhang, X. Y., Li, S. P., Yang, B. Y., & Wang, N. F. (2020). Flow structures of over-expanded supersonic gaseous jets for deep-water propulsion. *Ocean Engineering*, *213*, 107611-107624. https://doi.org/10.1016/j.oceaneng.2020.107611